Supplemental Information

Biomimetic Liquid Metal Cell

*Jingyi Li,[ab] Mengwen Qiao,[ab] Minghui Guo,[a] Zerong Xing,[ab] Yunlong Bai,[ab] Ju Wang,[ab] Yujia Song,[ab] Ren Xu,[b] Xi Zhao, *[cd] Jing Liu*[ab]*

This PDF file includes:

Other Supplemental Information for this manuscript includes the following:

Supplemental Note 1: Selection of materials for metal cores

In this study, EGaIn was specifically selected as the core material due to its advantages in phase change behavior and property characterization. The melting point of EGaIn is approximately 15.7 °C. [1] This physical property falls perfectly within the temperature range of our experimental investigation. Under the current fabrication parameters, EGaIn can remain suspended at the central region of the cytoplasm during the freezing stage. It subsequently melts and settles to the bottom of the internal cavity upon rewarming. In the study of low temperature phase change behavior, EGaIn exhibits a phase transition that lags behind that of the surrounding solution matrix. In contrast, other alloys like Galinstan possess much lower melting points and remain liquid under most conditions within our experimental temperature window. Therefore, EGaIn is the optimal choice to systematically investigate the states of both liquid and solid cores in this proof of concept study.

However, it should be noted that the fabrication strategy developed in this paper serves as a versatile platform capable of encapsulating various functionalized alloys. It is not limited by shape, structure, or specific alloy composition. The EGaIn-based LMC presented in this work serves as a representative model, and the platform can be readily extended to encapsulate other liquid metal alloys for customized functionalities.

Supplemental Note 2: Crosslinking mechanism and stability of the composite membrane

During precursor preparation, the water-soluble PEDOT:PSS is first dissolved in deionized water,[2] and sodium alginate is subsequently dissolved in this solution to yield a homogeneous precursor. [3] When this precursor contacts the calcium lactate solution, Ca^{2+} ions crosslink the guluronic acid residues (G-blocks) of the alginate chains to form the water-insoluble "egg-box" structure, [4] establishing a three-dimensional hydrogel network. As only the alginate is crosslinked while the PEDOT:PSS chains remain linear, the resulting structure constitutes a semi-interpenetrating polymer network (semi-IPN) in which PEDOT:PSS is physically entrapped within the dense calcium alginate matrix.[5] Hydrogen bonding and electrostatic interactions between the polymer chains further restrict the segmental mobility of PEDOT:PSS. These topological and intermolecular constraints effectively prevent the macroscopic leaching of PEDOT:PSS into the surrounding aqueous environment, ensuring the long-term stability of the composite membrane. [6]

To minimize experimental variables, all data presented in the main text were collected using LMCs within 2 hours of fabrication. Throughout all dynamic experiments, including the electrical and magnetic tuning tests conducted in 0.5 mol/L NaOH solutions, the LMCs maintained excellent structural integrity without membrane rupture or PEDOT:PSS leakage.

Beyond the operational timescale, storage tests were conducted to evaluate the practical stability of LMCs. Intact LMCs stored in 0.005 mol/L NaOH solution at 3 °C for 24 hours fully maintained their structural integrity (**Fig. S1A**). Although the liquid metal core naturally oxidizes in dilute NaOH, it rapidly recovers its original morphology and electrical responsiveness once transferred back to the operational NaOH concentration (0.5 mol/L). Over a longer period, composite hydrogel samples stored in deionized water at 3 °C for 6 months perfectly retained their original blue color and structural integrity (**Fig. S1B**). The surrounding water remained clear and did not turn blue, confirming that no macroscopic leaching of PEDOT:PSS occurred.

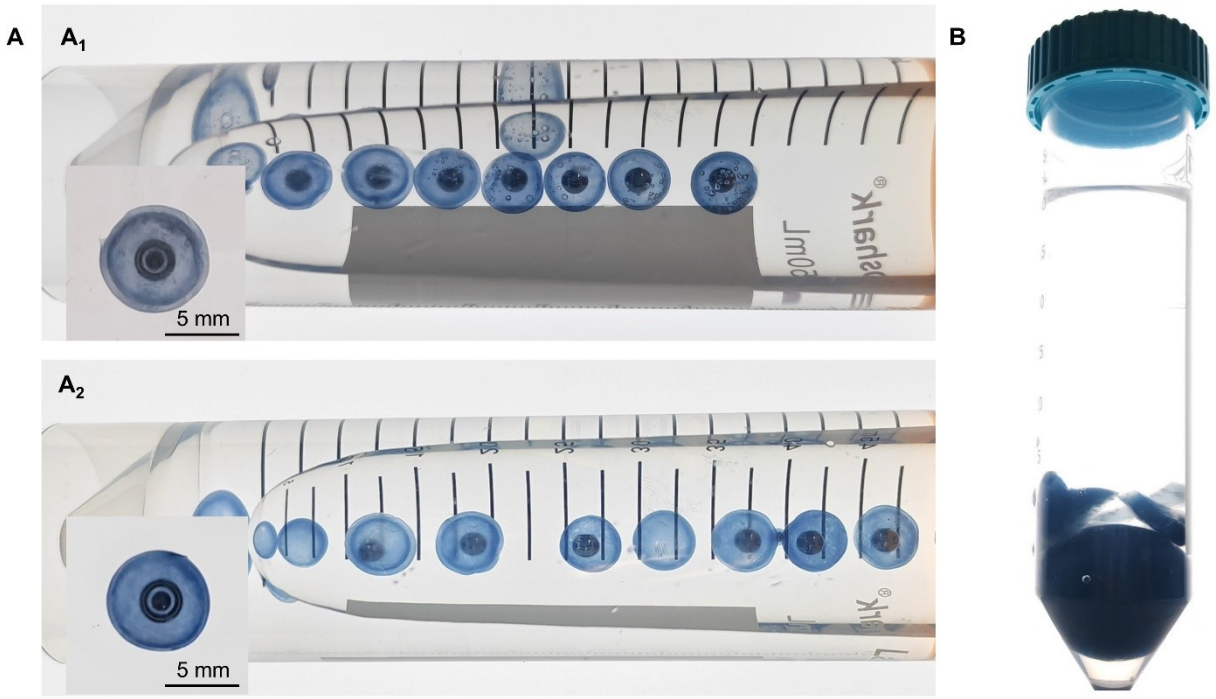

Supplemental Figure 1. Stability of liquid metal cells in aqueous environments. A. Short-term stability of liquid metal cells: A_1. Freshly prepared LMCs; A_2. LMCs stored in 0.005 mol/L sodium hydroxide solution for 24 hours; B. Composite gel sample stored in DI water for 6 months.

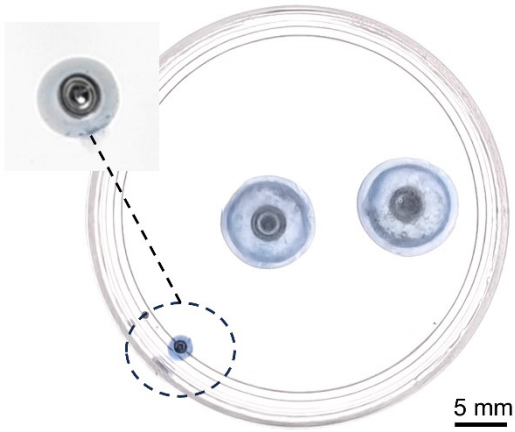

Supplemental Figure 2. Comparison between the selected size of LMCs and the smallest manufactured LMC (approximately 2 mm in diameter).

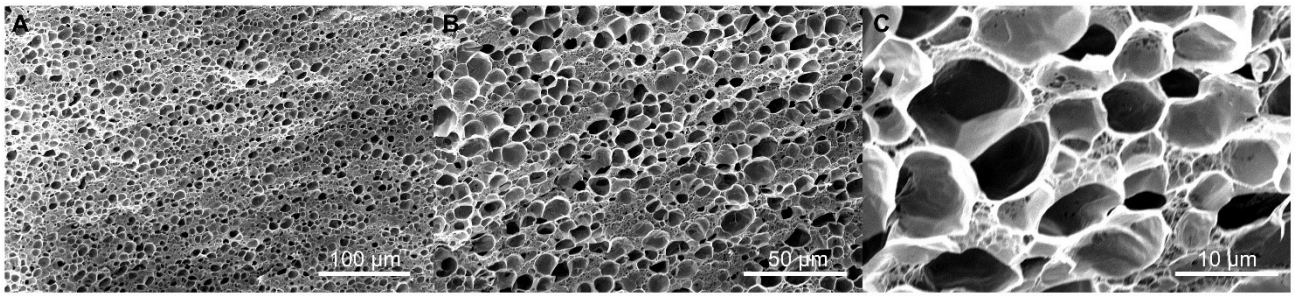

Supplemental Figure 3. Cross-sectional morphological characterization of the hydrogel layer. A. 441× magnification; B. 100× magnification; C. 5000× magnification.

With increasing compression distance, the stress experienced by the LMCs gradually increased, exhibiting a more pronounced stress growth rate in the later stages of compression compared to unfilled vesicular structures without liquid metal cores.

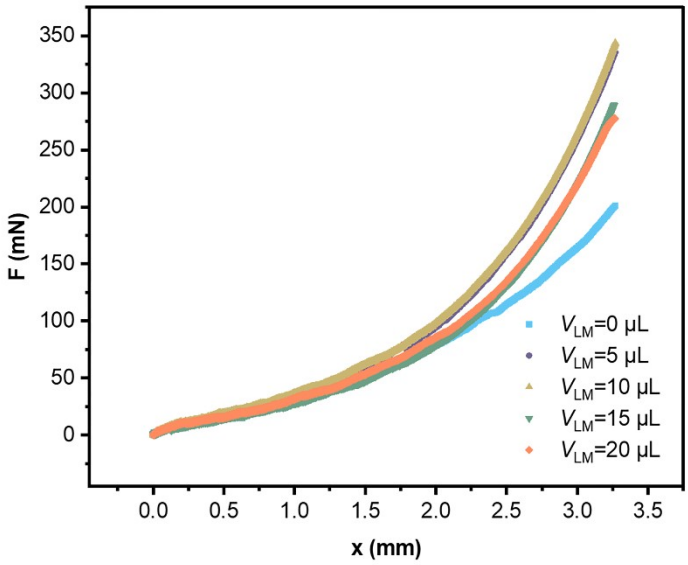

Supplemental Figure 4. Stress-strain curves of LMCs with different metal core contents.

Supplemental Note 3: Resistance model of the LMC

To calculate the electrical resistance from the top electrode to the bottom electrode, we need to consider the specific paths that the current can take through the composite structure of the LMC. We simplify the resistance model of the LMC to a configuration where a liquid metal droplet is deposited at the bottom of a solution sphere, and together they are encapsulated by an outer hydrogel spherical shell.

Since the electric conductivity of the liquid metal is much higher than that of the solution ($\sigma_{EGaIn} = 3.4 \times 10^6\ S/m,\ \sigma_{NaOH\ Solution} = 9.31\ S/m$), [7] the resistance of the solution pathway through the liquid metal droplet is necessarily less than the resistance of the solution that follows a longer path away from the centerline. Therefore, we only consider the solution resistance between the top electrode and the upper surface plane of the liquid metal droplet as the modeling object. Due to gravity and distance constraints between the two electrode plates, the LMC cannot maintain a perfect spherical structure and the contact area between the LMC and the electrode plate, A_T, must be considered when building the resistance model (**Fig. S5**). Therefore, we further simplify the effective current pathway to a truncated cone and treat the hydrogel spherical shell at the contact area with the electrode plate as a hydrogel layer with a thickness of t_h.

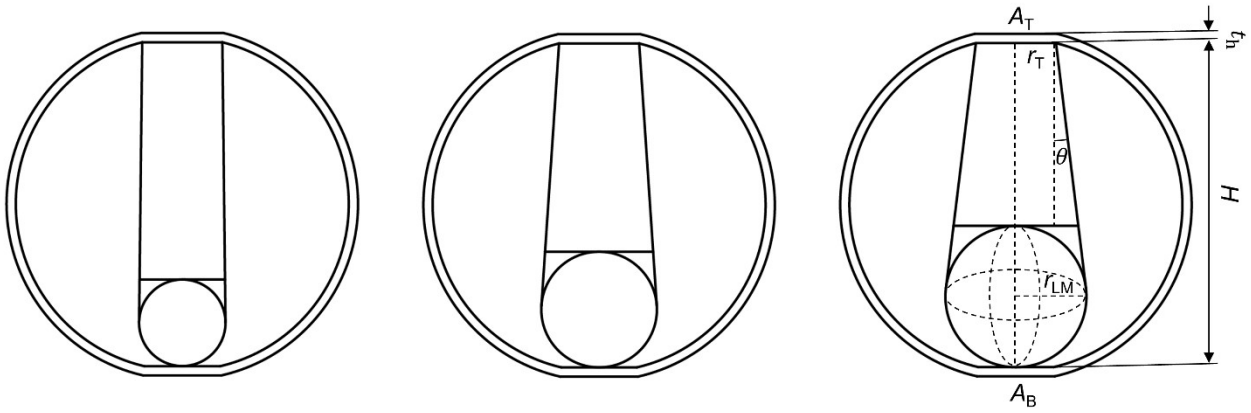

Supplemental Figure 5. Simplified model of LMCs with increasing nuclear fraction. The separation angle θ cutting angle increases significantly with increasing liquid metal content.

The resistance of the LMC (R_{LMC}) can be finally calculated as:

$R_{LMC} = R_s + R_{LM} + R_h \#(S1)$

where R_s is the resistance of the truncated cone-shaped solution part, R_{LM} is the resistance of the liquid metal droplet, and R_h is the resistance of hydrogel.

Resistance of the truncated cone-shaped solution part (R_s)

We consider it as being composed of an infinite number of thin disks stacked upon each other, with each disk's radius varying with height. By employing the method of integration, we can determine R_s:

$$R_s = \int_0^{H-2r_{LM}} \frac{dz}{\pi\sigma_s(r_T + z\tan\theta)^2}$$

$$= \int_{r_T}^{r_T+\tan\theta(H-2r_{LM})} \frac{dr}{\pi\sigma_s \tan\theta r^2} = -\frac{1}{\pi\sigma_s r\tan\theta}\Big|_{r_T}^{r_T+\tan\theta(H-2r_{LM})}$$

$$= \frac{1}{\pi\sigma_s r_T}\frac{H-2r_{LM}}{(r_T+\tan\theta(H-2r_{LM}))} = \frac{1}{\pi\sigma_s r_T}\frac{1}{\frac{r_T}{H-2r_{LM}}+\tan(\sin^{-1}\frac{r_{LM}}{H-r_{LM}})} \#(S2)$$

where σ_s is the electric conductivity of the solution, r_{LM} is the radius of the liquid metal droplet, r_T is the radius of the top surface of the truncated cone (where it contacts the hydrogel), and H is the inner high of the hydrogel shell, θ is the separation angle ($\sin\theta = \frac{r_{LM}}{H-r_{LM}}$).

Resistance of liquid metal droplet resistance (R_{LM}):

$$R_{LM} = \frac{1}{4\pi\sigma_{LM} r_{LM}} \#(S3)$$

where $\sigma_{LM}$is the electric conductivity of the liquid metal.

Resistance of hydrogel part (R_h):

$$R_h = \frac{t_h}{\sigma_h}\left(\frac{1}{A_T}+\frac{1}{A_B}\right) \#(S4)$$

where σ_h is the electric conductivity of the hydrogel, $t_h$is the thickness of the shell, A_T is the contact area between the hydrogel layer and the top electrode, and A_B is contact area between the hydrogel layer and the bottom electrode.

In summary, the resistance of the LMC can be expressed as:

$$R_{LMC} = \frac{1}{\pi\sigma_s r_T}\frac{1}{\frac{r_T}{H-2r_{LM}}+\tan(\sin^{-1}\frac{r_{LM}}{H-r_{LM}})} + \frac{1}{4\pi\sigma_{LM} r_{LM}} + \frac{t_h}{\sigma_h}\left(\frac{1}{A_T}+\frac{1}{A_B}\right) \#(S5)$$

Theoretical modeling demonstrates that with the increasing proportion of liquid metal, r_{LM} exhibits monotonic decrease, while R_s shows monotonic decrease within the range of $\theta < 90°$. The maximum V_{LM} of 20 μL observed in our experiments corresponds to θ ranging from 18.476° to 54.982° during the compression process, which falls within the applicable scope of the theoretical model.

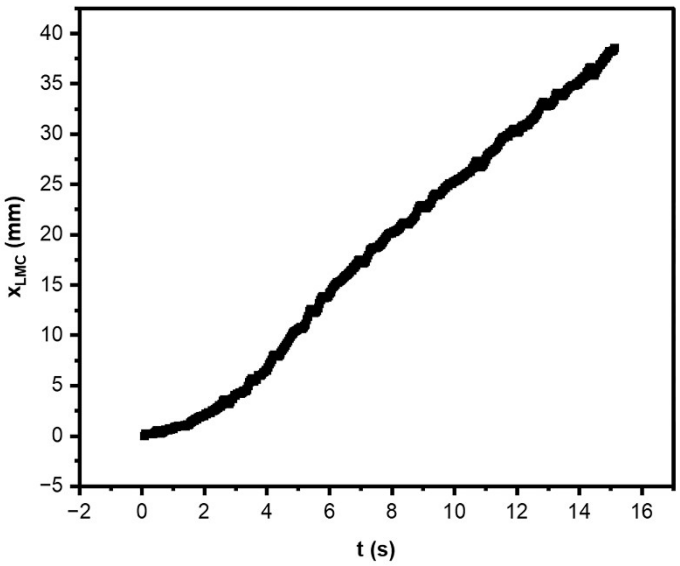

Supplemental Figure 6. The complete motion process of the LMC ($V_{LM} = 10\ \mu L$). After experiencing a transient acceleration phase, the system achieves and maintains a steady-state uniform velocity.

Supplemental Note 4：Analysis of the motion characteristics of the LMC under an electric field

The force analysis focuses mainly on the LMC nucleus, it is primarily subjected to forces resulting from surface tension imbalance (F_γ), viscous drag caused by the surrounding solution (f_η), and frictional forces from the hydrogel membrane at the bottom (f_β). It can be seen from the schematic that f_η and f_β are the resisting forces, while F_γ is the only driving force (**Fig. S7**). [8]

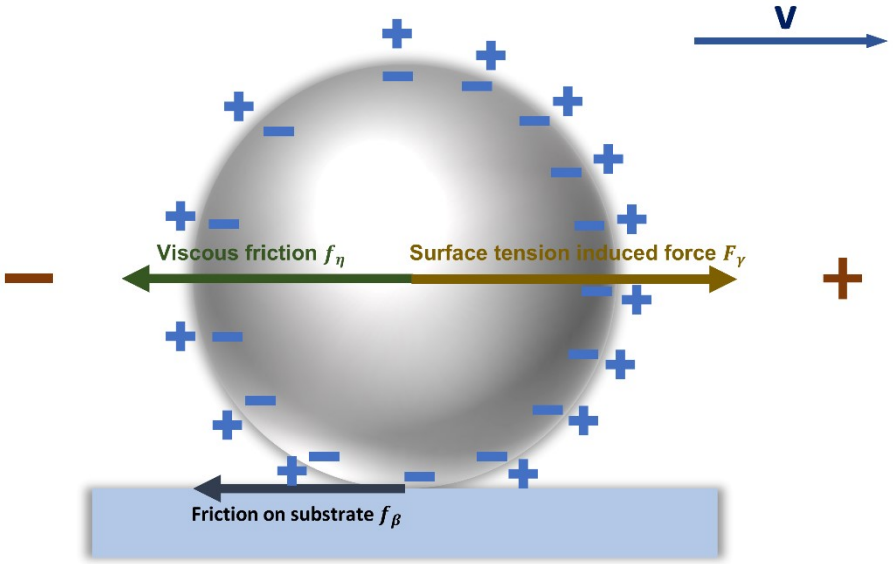

Supplemental Figure 7. Analysis of lateral forces on the liquid metal drop in a LMC under the influence of external potential difference, assuming the liquid metal droplet is spherical, the gas produced by electrolysis is neglected.

The surface tension induced driving force of the droplet originates from an electric field that induces an asymmetric electric double layer. This asymmetry leads to a difference in surface tension, which subsequently results in a pressure difference.

Lippmann Equation describes the relationship between interfacial tension and applied voltage at the liquid metal-electrolyte interface, indicating how the surface tension varies with electric potential:

$$\gamma = \gamma_0 - \frac{c}{2}U^2 \#(S6)$$

And *Young-Laplace Equation* governs the pressure difference across the liquid metal-electrolyte interface, relating it to surface tension and interface curvature:

$$p = \frac{2\gamma}{r} \#(S7)$$

These equations explain how electric field induces movement of liquid metal droplets through electrocapillary effects.

The pressure difference across the left and right sides of the liquid metal droplet(Δp) is obtained as：

$$\Delta p = p_L - p_R = \frac{2(\gamma_L - \gamma_R)}{r} = \frac{2\Delta\gamma}{r} \#(S8)$$

The surface tension difference across the left and right sides of the liquid metal droplet ($\Delta\gamma$) is:

$$\Delta\gamma = \gamma_L - \gamma_R = \frac{c\left(U_R^2 - U_L^2\right)}{2} \#(S9)$$

The voltage difference between the left and right sides of the droplet (U_L and U_R) arises from the differing electric potentials at these positions within the electric field. To calculate the potential difference across the droplet, one can estimate based on the positions of the droplet's sides, the resistance values of the liquid metal, and the solution within the channel. Given that the resistance of the liquid metal is negligible compared to that of the solution, here we only consider the resistance of the solution between the left and right positions of the droplet.

Assuming the potential difference across the entire droplet is $\Delta\varphi$, the electric potentials on the left and right sides can be expressed as:

$$U_L = U_0 - \frac{\Delta\varphi}{2} \#(S10)$$

$$U_R = U_0 + \frac{\Delta\varphi}{2} \#(S11)$$

where U_0 is the potential difference of the symmetric electric double layer on the surface of the liquid metal in the absence of an applied electric field.

Since the electric double layer can be considered as a capacitor *c* with a charge q_0, there is:

$$U_0 = \frac{q_0}{c} \#(S12)$$

By substituting the relevant expressions from Eq. S10 and Eq. S11 into the Eq. S9, we obtain the following relationship：

$$\Delta\gamma = \gamma_L - \gamma_R = \frac{c\left(U_R^2 - U_L^2\right)}{2} = \frac{c(U_R + U_L)(U_R - U_L)}{2} = \frac{2cU_0\Delta\varphi}{2} = cU_0\Delta\varphi \#(S13)$$

Substituting Eq. S12 into the above expression, we obtain:

$$\Delta\gamma = q_0\Delta\varphi \#(S14)$$

$$\Delta p = \frac{2q_0\Delta\varphi}{r_{LM}} \#(S15)$$

where r_{LM} is radius of the liquid metal droplet.

Next, based on the voltage division rule for series resistances, we derive the potential difference across the droplet ($\Delta\varphi$):

$$\Delta\varphi = IR_d = \frac{U_E}{R_t}R_d = \frac{U_E}{\frac{L_E}{\sigma_S S_E}}R_d \#(S16)$$

where I is the current between the two electrodes, R_d is the resistance of the solution enclosed between the left and right sides of the liquid metal droplet and the channel, U_E is the potential difference between the electrodes on either side, R_t is the total resistance of the solution between the two electrodes, L_E is distance between two electrodes，σ_S is the electric conductivity of the solution, and S_E is the cross-sectional area of the solution portion.

Here, we simplify the portion of the solution constrained by the two sides of the droplet into a cuboid with a length of $2^{r_{LM}}$ and an equivalent cross-sectional area of S_d，

$$S_d = \frac{2r_{LM}h_1h_2 - \frac{4}{3}\pi r_{LM}^3}{2r_{LM}} = h_1h_2 - \frac{2}{3}\pi r_{LM}^2 \#(S17)$$

$$R_d = \frac{2r_{LM}}{\sigma_S S_d} = \frac{2r_{LM}}{\sigma_S\left(h_1h_2 - \frac{2}{3}\pi r_{LM}^2\right)} \#(S18)$$

where h_1 and h_2 are the width and height of the channel filled with liquid, respectively.

Substituting Eq. S18 into Eq. S16, we obtain:

$$\Delta\varphi = \frac{U_E}{\frac{L_E}{\sigma_S S_E}\sigma_S\left(h_1h_2 - \frac{2}{3}\pi r_{LM}^2\right)}\frac{2r_{LM}}{} = \frac{2U_E h_1h_2 r_{LM}}{L_E\left(h_1h_2 - \frac{2}{3}\pi r_{LM}^2\right)} \#(S19)$$

Substituting Eq. S19 into Eq. S15, we obtain:

$$\Delta p = \frac{2q_0\Delta\varphi}{r_{LM}} = \frac{4q_0U_E S_E}{L_E S_d} = \frac{4q_0U_E h_1h_2}{L_E\left(h_1h_2 - \frac{2}{3}\pi r_{LM}^2\right)} \#(S20)$$

Integrating over the entire droplet, we obtain:

$$F_\gamma = \int_0^\pi\int_0^\pi \Delta p r_{LM}^2 \sin\theta \sin^2\varphi d\theta d\varphi = \pi r_{LM}^2\Delta p$$
$$= \frac{4q_0U_E h_1h_2}{L_E\left(\frac{h_1h_2}{\pi r_{LM}^2} - \frac{2}{3}\right)} = \frac{4q_0U_E}{L_E\left(\frac{1}{\pi r_{LM}^2} - \frac{2h_1h_2}{3}\right)} \#(S21)$$

Supplemental Figure 8. Response behavior of the LMC and a liquid metal droplet under an alternating current electric field. A. At 20 Hz, the metallic core within the LMC enters a resonant state; B. At 40 Hz, the droplet in the solution environment enters a resonant state.

Supplemental Note 5：Passive motion synchronization of the magnetic LMC

To characterize the motion synchronization of Magnetic LMCs under magnetic guidance, we capture the movement of LMCs following a circular magnet using high-speed videography at 500 fps (**Fig. S9A**) (. When performing outward spiral motion with gradually increasing radius (**Fig. S9B**), we observed an average position correlation coefficient of 0.91 between the LMC and the guiding magnet, which increased to above 0.99 during the linear segments.

During motion, the internal liquid metal magnetofluid closely tracks the circular magnet beneath the container, driving the overall LMC movement. At points of rapid directional change, inertial lag of the external polymer membrane causes the liquid metal core to undergo relative positional displacement within the LMC structure (**Fig. 4E**). This displacement results in transient increases in the center-to-center distance between the LMC and the magnet (**Fig. S9C**), accompanied by corresponding decreases in motion correlation. This phenomenon provides additional evidence for the structural flexibility of LMC components during locomotion.

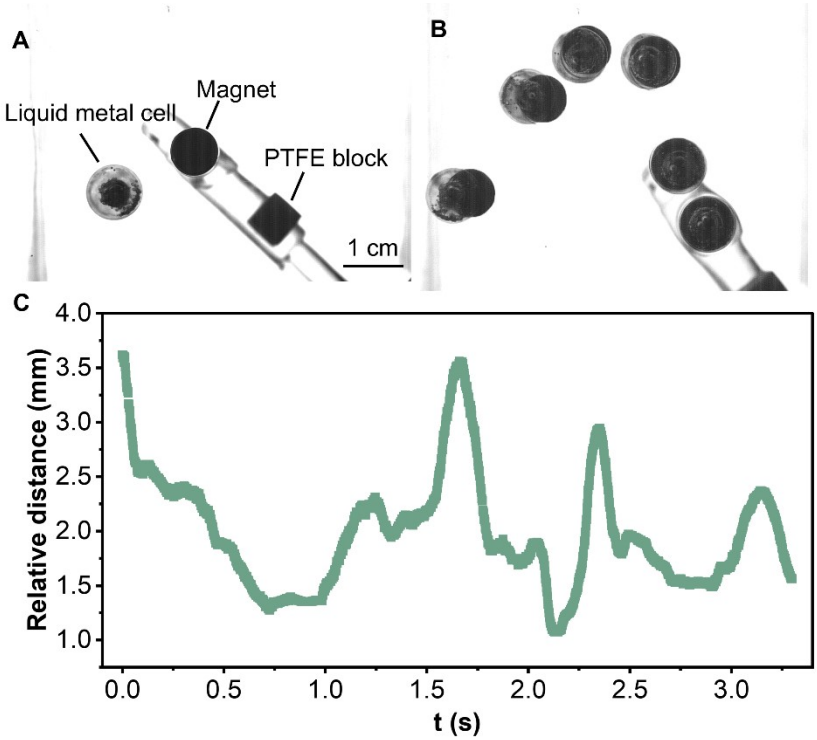

Supplemental Figure 9. Motion of magnetic LMCs under magnetic guidance. A. Magnetic LMC positioned in a solution environment with a circular magnet beneath the container. B. Motion trajectories of the magnetic LMC and the guiding magnet. C. Relative distance variation between the magnetic LMC and the magnet.

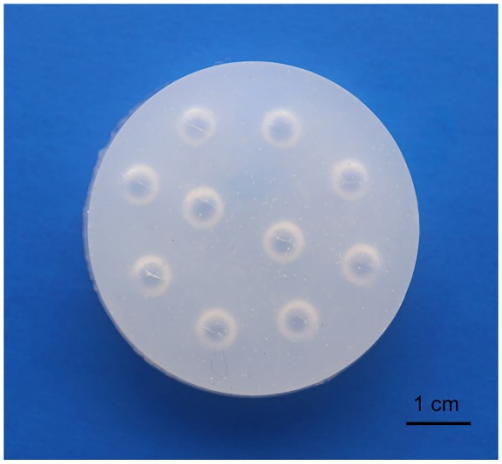

Supplemental Figure 10. The mold for constructing the cytoplasm-nucleus composite structure (inner cavity diameter= 7 mm) in LMCs. The mold was constructed utilizing Ecoflex 00-30.

Supplemental Note 6: Statistical analysis

From our statistical analysis of 30 sample groups of LMCs, the average membrane thickness was 0.207833 mm with a variance of 0.003639 mm^2. Statistical analysis of 274 pores (from 5 replicates) in the composite hydrogel membrane section revealed an average pore size of 7.876 ± 1.910 μm with a porosity of 81.568%. For the resistances in **Fig. 2C$_1$**, **Fig. 2D**, **Fig. 2E**, and **Fig. 3**, as well as the activation voltages and velocity in **Fig. 4B**, we performed n=5 independent replicates to ensure statistical significance. The error bars in these figures represent the standard deviation (±SD), and each dataset was calculated by Origin. The investigators were not blinded to allocation during experiments and outcome assessment.

References

1. D. Zrnic and D. Swatik, *Journal of the Less Common Metals*, 1969, **18**, 67–68.
2. B. Lu, H. Yuk, S. Lin, N. Jian, K. Qu, J. Xu and X. Zhao, *Nature Communications*, 2019, **10**, 1043.
3. K. Zhao, Y. Zhao, J. Xu, R. Qian, Z. Yu and C. Ye, *Chemical Engineering Journal*, 2024, **494**, 152971.
4. G. T. Grant, E. R. Morris, D. A. Rees, P. J. C. Smith and D. Thom, *FEBS Letters*, 1973, **32**, 195–198.
5. P. Matricardi, C. Di Meo, T. Coviello, W. E. Hennink and F. Alhaique, *Advanced Drug Delivery Reviews*, 2013, **65**, 1172–1187.
6. L. Ferlauto, A. N. D'Angelo, P. Vagni, M. J. I. Airaghi Leccardi, F. M. Mor, E. A. Cuttaz, M. O. Heuschkel, L. Stoppini and D. Ghezzi, *Frontiers in Neuroscience*, 2018, **12**, 648.
7. W. M. Haynes, *CRC Handbook of Chemistry and Physics*, CRC press, 2016.
8. M. F. Wang, M. J. Jin, X. J. Jin and S. G. Zuo, *Physical Chemistry Chemical Physics*, 2017, **19**, 18505–18513.